J Adv Ceram

Research Article

Synthesis of ultralight hollow SiC/C nanofiber for highly efficient electromagnetic wave absorption

Yun-Tian Chen[1,2], Hualong Peng[1,2], Bo Cai[1,2], Chen-Ming Liang[1,2], Yu Zhang[1,2], Pei-Yan Zhao[1,2]✉, Pengfei Hu[3], Wen-Ping Li[4]✉, Guang-Sheng Wang[1,2]✉

Cite this article: Chen Y, Peng H, Cai B, et al. *J Adv Ceram* 2026, **15**(2): 9221225. https://doi.org/10.26599/JAC.2025.9221225

ABSTRACT: The development of multifunctional electromagnetic wave-absorbing materials capable of operating in complex environments has become critically important in the field of electromagnetic protection. However, achieving materials that combine high absorption efficiency with exceptional thermal stability remains a significant challenge. Owing to their lightweight hollow structure, low thermal conductivity, and high thermal stability, hollow SiC/C fibers present a promising solution to the problem of high-temperature electromagnetic wave absorption. In this study, hollow SiC/C nanofibers were successfully synthesized via a combined hydrothermal and carbothermal reduction approach. The resulting hollow SiC/C nanofibers exhibit ultralight characteristics, high-temperature stability, good elasticity and fatigue resistance, and exceptional electromagnetic wave absorption performance, including an effective absorption bandwidth of 7.0 GHz at a thickness of 2.4 mm and an optimal reflection loss of −63.5 dB at a thickness of 1.4 mm. Moreover, the material demonstrates remarkable high-temperature dielectric stability, with its complex permittivity remaining virtually unchanged at 600 °C. The formulated strategy provides a feasible approach for designing SiC matrix composites with stable dielectric properties and efficient electromagnetic wave absorption.

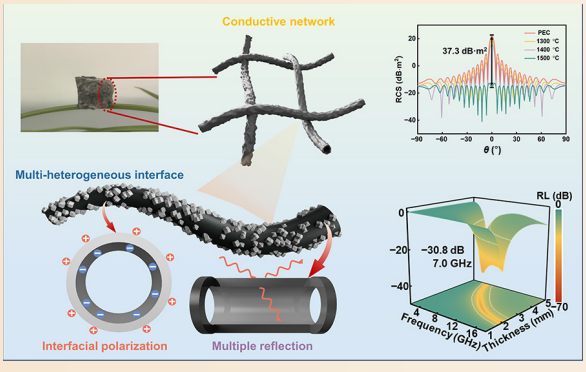

KEYWORDS: silicon carbide; hollow nanofibers; broad bandwidth; electromagnetic wave absorption

1 Introduction

With the advancements in military equipment and civilian facilities, electromagnetic wave protection materials are increasingly subjected to harsh service conditions, such as high temperatures, oxygen-rich environments, and high humidity [1]. Consequently, the development of multifunctional electromagnetic wave absorbing materials capable of operating in complex environments has become critically important [2–5]. From a practical application perspective, composites featuring hierarchical architectures or hollow cavities are considered promising candidates for high-temperature electromagnetic wave absorption because of their ultrahigh porosity, low thermal conductivity, optimized impedance matching, synergistic electromagnetic effects, and multiple heterogeneous interfaces [6,7]. Moreover, the hollow structure can effectively reduce the density of the material, which is conducive to meeting the requirements of the new generation of absorbing materials. However, such hollow-structured composites often suffer from complex fabrication processes and uncontrollable microstructures. Thus, developing a straightforward synthesis strategy to precisely control hollow structures remains an urgent and challenging research problem.

Carbon materials are widely employed in electromagnetic wave absorption applications because of their lightweight nature, high melting point, strong electromagnetic wave dissipation capacity, and ease of fabrication [8]. Researchers often introduce magnetic or dielectric components into carbon matrices to reduce the disparity between permittivity and permeability, thereby optimizing impedance matching characteristics [4]. However, under high-temperature service conditions, carbon materials not only undergo oxidation to CO_2 but also cause the magnetism of the incorporated magnetic components to decrease upon exceeding the Curie temperature, leading to impedance mismatch. Therefore, introducing dielectric materials with high-temperature stability and strong oxidation resistance into carbon matrices is considered a promising approach to address the high-temperature failure of carbon-based absorbers [9]. Silicon carbide (SiC), a

[1] State Key Laboratory of Bioinspired Interfacial Materials Science, Bioinspired Science Innovation Center, Hangzhou International Innovation Institute, Beihang University, Hangzhou 311115, China. [2] School of Chemistry, Beihang University, Beijing 100191, China. [3] Research Institute of Aero-Engine, Beihang University, Beijing 100191, China. [4] School of Physics, Beihang University, Beijing 100191, China.

✉ Corresponding authors. E-mail: P.-Y. Zhao, zhaopy@buaa.edu.cn; W.-P. Li, liwp@buaa.edu.cn; G.-S. Wang, wanggsh@buaa.edu.cn

Received: September 28, 2025; Revised: November 17, 2025; Accepted: November 28, 2025

typical wide-bandgap semiconductor (e.g., E_g = 3.26 eV for 4H-SiC), has emerged as a cornerstone material for advanced electromagnetic applications because of its excellent mechanical hardness, corrosion resistance, and high-temperature stability [10–12]. Through silicon vapor deposition, SiC can be generated in situ on a carbon substrate, consuming graphitic carbon to optimize impedance matching while concurrently enhancing the oxidation resistance and thermal stability of the matrix and creating abundant heterogeneous interfaces to improve polarization loss and overall absorption performance [13–15]. However, the density of silicon carbide is significantly greater than that of pyrolytic carbon. The introduction of SiC alone reduces the light weight advantage of carbon-based absorbing materials. Therefore, the construction of hollow-structured SiC/C composites is expected to provide an effective solution to the challenge of high-temperature wave absorption.

In this study, we fabricated hierarchical hollow SiC/C nanofibers (H-SiC/C NFs) using AgNW@PVA as a substrate through a combination of a hydrothermal reaction and silicon vapor infiltration. By precisely controlling the reaction conditions, we regulated the SiC/C ratio and hollow architecture of the fibers, thereby clarifying the corresponding evolution of their electromagnetic properties. The aerogel was constructed from continuously wound one-dimensional H-SiC/C NFs, which simultaneously overcomes the intrinsic brittleness of traditional ceramic aerogels and exhibits exceptional elasticity and fatigue resistance. Furthermore, the material demonstrates remarkable high-temperature dielectric stability, maintaining consistent electrical properties even when heated to 600 °C, which is a critical advantage for applications in extreme thermal environments. The hollow structure not only optimizes the impedance matching but also enhances the interfacial polarization, significantly broadening the effective absorption bandwidth. The H-SiC/C NF composites exhibited excellent electromagnetic wave absorption performance, achieving an effective absorption bandwidth of 7.0 GHz (11–18 GHz) at a thickness of 2.4 mm and an optimal reflection loss of −63.5 dB at a thickness of 1.4 mm. This work provides a paradigm for high-performance electromagnetic wave absorbers suitable for high-temperature applications, demonstrating the effectiveness of hollow structures in optimizing impedance, which offers valuable guidance for designing high-temperature electromagnetic wave absorption materials.

2 Materials and methods

2.1 Materials

Polyvinyl alcohol (PVA 1799, alcoholysis degree 98%–99%) and sodium chloride (NaCl, analytical grade) were obtained from Shanghai Macklin Biochemical Co., Ltd. Silver nitrate ($AgNO_3$, analytical grade) was supplied by Guanghua Chemical Reagent Co., Ltd. Nanoscale silicon powder (Si, 99.9%, 80–120 nm) was provided by Xinnai Metal Materials Co., Ltd. Paraffin (99% purity) was purchased from Modern Oriental (Beijing) Technology Development Co., Ltd. High-purity argon (Ar, 99.9992%) was provided by Beijing Qianxi Jingcheng Gas Co., Ltd.

2.2 Preparation of H-SiC/C NFs

The synthesis process of the H-SiC/C NFs consisted of two steps: a hydrothermal reaction and silicon vapor infiltration (SVI). First, 5.4 g of PVA 1799 was dissolved in 671 mL of water at 85 °C under constant stirring to form a clear solution. Then, 0.3 g of NaCl and 3 g of $AgNO_3$ were added and mixed for 30 min. The resulting solution was transferred into a Teflon-lined stainless-steel autoclave and hydrothermally reacted at 160 °C for 65 h. The brown flocculent precipitate was collected, gently washed five times with distilled water, and freeze-dried to obtain a silver nanowire@polyvinyl alcohol (AgNW@PVA) aerogel. The aerogel was mixed with nanosilicon powder, placed in an alumina crucible, and annealed at 1300–1500 °C for 2 h under flowing argon. The resulting H-SiC/C NFs were designated S1300–S1500 on the basis of their respective synthesis temperatures. The influence of the precursor C/Si ratio on the morphology and properties of the H-SiC/C nanofibers was investigated for samples heat-treated at 1500 °C. The samples with C/Si ratios of 5 : 1, 7 : 1, and 9 : 1 were labeled S1500-51, S1500-71, and S1500-91, respectively.

2.3 Characterizations

The crystalline structures and phase compositions were characterized via an X-ray diffractometer (XRD; Rigaku Smartlab SE, Japan) using Cu Kα radiation. The microstructure was examined via a field-emission scanning electron microscope (FE-SEM; JSM 7500F, Japan) and a transmission electron microscope (TEM; Tecnai G2 F30 S-TWIN, FEI, USA). The elemental distribution and compositional homogeneity were analyzed via an energy-dispersive X-ray spectroscope (EDS; Thermo Axia ChemiSEM, USA). The degree of carbonization of the H-SiC/C NFs was evaluated via a Raman spectroscope (LabRAM HR Evolution, HORIBA, Japan). The surface chemical states were investigated via an X-ray photoelectron spectroscope (XPS; Thermo Fisher EscaLab 250Xi, USA). Thermal stability was assessed via a thermogravimetric analyzer (TGA; STA 449F5, Netzsch, Germany) under a nitrogen atmosphere from ambient temperature to 1300 °C at a heating rate of 10 °C/min. The contents of Si and Ag were quantified via inductively coupled plasma-optical emission spectrometry (ICP-OES, Agilent 5110, USA). Surface potential measurements of H-SiC/C NFs were performed with a Kelvin probe force microscope (KPFM, Bruker Dimension Icon, Germany).

Electromagnetic parameter characterization: The electromagnetic properties were measured via a vector network analyzer (VNA; ZNA43, ROHDE & SCHWARZ, Germany) via the coaxial-line method within the gigahertz frequency range. Test samples were prepared by uniformly mixing the H-SiC/C NFs with paraffin wax, followed by compression molding into toroidal shapes with inner and outer diameters of 3.04 and 7.00 mm, respectively. To evaluate the influence of filler content on electromagnetic performance, composites with filler loadings ranging from 13 to 17 wt% (in increments of 2 wt%) were systematically investigated. For the high-temperature dielectric test, the hollow SiC/C nanofibers were uniformly blended with SiO_2 powder at an equal volume ratio. The mixture was then uniaxially pressed into a rectangular block measuring 22.8 mm × 10.1 mm × 2.0 mm (to fit the X-band waveguide) and subsequently heat-treated at 800 °C to ensure structural stability. The density of the prepared sample was 1.01 g/cm^3. The complex permittivity was measured across the X-band (8.2–12.4 GHz) and a temperature range of 20–600 °C via the waveguide method using a vector network analyzer (VNA; 3672B-S, Ceyear, China). Prior to testing, the VNA was carefully calibrated, and a 20-min dwell time was implemented at each target temperature to ensure thermal equilibrium and measurement accuracy.

Electromagnetic wave absorption performance assessment: The electromagnetic wave absorption capability was evaluated on the basis of the reflection loss (RL) derived from transmission line theory (Eqs. (1) and (2)) [16,17]:

$$RL = 20\log\left|\frac{Z_{in} - Z_0}{Z_{in} + Z_0}\right| \quad (1)$$

$$Z_{in} = Z_0\sqrt{\frac{\mu_r}{\varepsilon_r}}\tanh\left(j\left(\frac{2f\pi d}{c}\right)\sqrt{\mu_r\varepsilon_r}\right) \quad (2)$$

where Z_{in} denotes the input impedance of the materials, and Z_0 denotes the intrinsic impedance of free space (377 Ω). RL, ε_r, μ_r, f, d, and c represent the reflection loss, the complex permittivity, the complex permeability, the frequency of the electromagnetic wave, the material thickness, and the speed of light in vacuum, respectively.

Impedance matching plays a critical role in governing the penetration of incident electromagnetic waves into the absorber. This property was quantified via the normalized characteristic impedance (M_z) [18], which is defined as Eq. (3):

$$M_z = \frac{2Z'_{in}}{|Z_{in}|^2 + 1} \quad (3)$$

where Z'_{in} is the real normalized input impedance.

The electromagnetic energy dissipation capability was quantified by the attenuation constant (α), with higher values indicating enhanced attenuation performance (Eq. (4)) [19,20]:

$$\alpha = \frac{\sqrt{2}}{c}\pi f \times \sqrt{(\mu''\varepsilon'' - \mu'\varepsilon') + \sqrt{(\mu''\varepsilon'' - \mu'\varepsilon')^2 + (\mu'\varepsilon'' + \mu''\varepsilon')^2}} \quad (4)$$

where ε', ε'', μ', μ'' represent the real part of the permittivity, the imaginary part of the permittivity, the real part of the permeability, the imaginary part of the permeability, respectively. Dielectric polarization behavior under alternating electromagnetic fields was analyzed via Cole–Cole plots on the basis of modified Debye theory [21,22], where each distinct polarization process is represented by a semicircular arc in the complex permittivity plane (Eqs. (5)–(7)):

$$\varepsilon' = \varepsilon_\infty + \frac{\varepsilon_S - \varepsilon_\infty}{1 + (2\pi f)^2\tau^2} \quad (5)$$

$$\varepsilon'' = \varepsilon_\infty + \frac{2\pi f\tau(\varepsilon_S - \varepsilon_\infty)}{1 + (2\pi f)^2\tau^2} = \varepsilon''_c + \varepsilon''_p \quad (6)$$

$$\varepsilon''_c = \frac{\sigma}{\omega\varepsilon_0} \quad (7)$$

where ε_s, ε_∞, ε_0, ε_c'', ε_p'', σ, τ, and ω are the static permittivity, the relative permittivity at the high-frequency limit, the vacuum permittivity (8.85×10^{-12} F/m), the conductive loss, the polarization loss, the electric conductivity, the relaxation time, and the angular frequency, respectively. The above two equations can be combined and represented as Eq. (8) [23]:

$$\left(\varepsilon' - \frac{\varepsilon_s + \varepsilon_\infty}{2}\right)^2 + (\varepsilon'')^2 = \left(\frac{\varepsilon_s - \varepsilon_\infty}{2}\right)^2 \quad (8)$$

On the basis of the quarter-wavelength cancellation theory, the influence of the macroscopic geometric structure on the dissipation of reflected electromagnetic waves can be evaluated via Eq. (9):

$$t_m = \frac{n\lambda}{4} = \frac{nc}{4f_m\sqrt{|\varepsilon_r|\,|\mu_r|}} \quad (n = 1, 3, 5\ldots) \quad (9)$$

where t_m and f_m represent the matching thickness and its corresponding peak frequency at the optimal RL value, respectively. $|\varepsilon_r|$ and $|\mu_r|$ are the moduli of the relative complex permittivity and permeability, respectively.

Finite element analysis: As shown in Fig. S1 in the Electronic Supplementary Material (ESM)), the H-SiC/C NF was constructed as a hollow cylinder (length: 6000 nm, radius: 265 nm, wall thickness: 65 nm). A perfectly matched layer (PML) boundary condition (radius: 15,000 nm) was employed to minimize nonphysical reflections. The computational domain was discretized via free tetrahedral elements to accommodate the complex geometry. The material was defined by importing its experimental frequency-dependent complex permittivity (ε_r), and a linearly polarized plane wave was used as the incident wave to evaluate the electromagnetic response. For the RCS simulation, the model was set up within a 312.8 mm × 312.8 mm × 17.8 mm vacuum domain, with radiation boundaries applied on all exterior surfaces. An automatic meshing technique was used for discretization, and the material was defined by importing the real part of the permittivity (ε') and the dielectric loss tangent ($\tan\delta_\varepsilon$) to ensure an accurate representation of its electromagnetic behavior.

3 Results and discussion

3.1 Preparation and characterization of H-SiC/C NFs

The synthetic route for the H-SiC/C NFs is schematically illustrated in Fig. 1(a), comprising three main steps: hydrothermal reaction, freeze-drying and SVI. The AgNW@PVA precursor was synthesized via a hydrothermal method. Under hydrothermal conditions, Ag ions coordinate with PVA, facilitating the detachment of hydrogen atoms from hydroxyl groups. This reaction promotes the formation of ether linkages between adjacent PVA chains, thereby inducing cross-linking [24]. Simultaneously, the Ag ions are reduced to metallic Ag nanoparticles. The cross-linked PVA serves as both a stabilizer and a structure-directing agent, passivating specific crystalline facets of the metallic Ag particles and guiding preferential growth along nonpassivated planes to form silver nanowires (AgNWs). These AgNWs constitute a continuous network around which crosslinked PVA chains are tightly wrapped, resulting in the formation of coaxial nanocable-structured AgNW@PVA. The AgNW@PVA aerogel was subsequently obtained through freeze-drying. As shown in Fig. S2 in the ESM, the intermediate AgNW@PVA aerogel consists primarily of well-defined coaxial nanocables with a Ag core and a PVA shell. These nanocables have diameters ranging from 100 to 800 nm and lengths of up to several hundred micrometres. They interweave and interconnect to form a three-dimensional porous aerogel architecture. This process provides the basic framework for our high-temperature heat treatment. Subsequent SVI processes convert the AgNW@PVA aerogel into interconnected H-SiC/C NFs. During heat treatment, the PVA shell is carbonized at 800 °C to form a carbonaceous layer. At elevated temperatures (1300–1500 °C), this carbon layer reacts with silicon vapor to form SiC grains via in situ carbothermal reduction. Concurrently, the AgNW core melts and evaporates, leaving behind a hollow architecture. This transformation is accompanied by a color change from brown to gray and slight volumetric contraction, yielding the final H-SiC/C NFs. The absence of Ag in the H-SiC/C NFs, as confirmed by ICP analysis (Table S1 in the ESM), indicates that the Ag core of the aerogel was completely volatilized and removed from the nanofibers during the high-temperature treatment. Figures 1(b)–1(g) presents SEM images of the H-SiC/C NFs obtained at

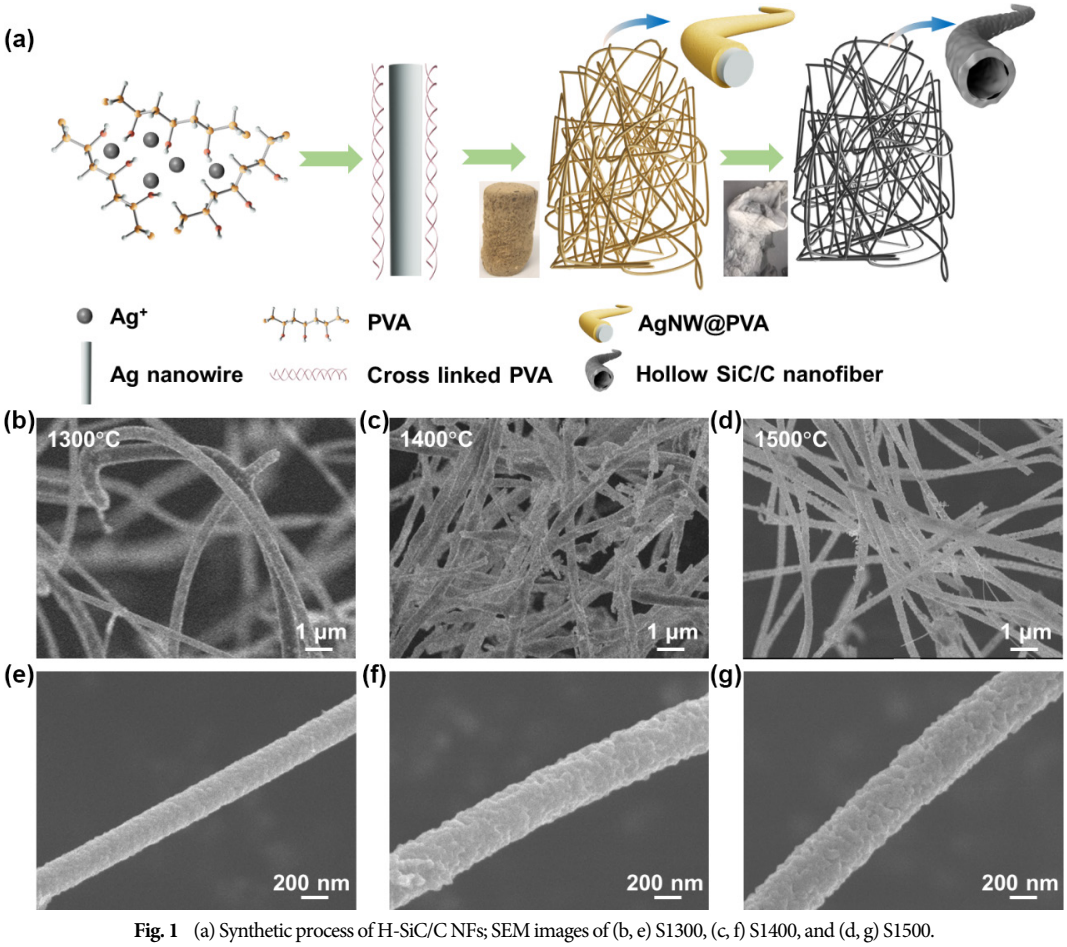

Fig. 1 (a) Synthetic process of H-SiC/C NFs; SEM images of (b, e) S1300, (c, f) S1400, and (d, g) S1500.

different heat treatment temperatures. Compared with that of the pristine AgNW@PVA nanocables, the surface of the SiC/C nanofibers was markedly rougher. As the temperature increases, the average fiber diameter increases, whereas the average length decreases, accompanied by a more distinct granular morphology on the shell. This evolution can be attributed to the temperature-dependent reaction kinetics between the silicon vapor and the carbonized shell of the nanocables, which governs the nucleation and growth rates of the SiC grains [25]. The *in situ* formation of SiC grains on the carbon shell contributes to the increase in diameter. Concurrently, the consumption of the carbonaceous matrix and the melting-volatilization of the Ag core at elevated temperatures led to fragmentation of a portion of the nanofibers, resulting in a reduction in their average length. Figure S3 in the ESM shows SEM images of H-SiC/C NFs prepared with different C/Si ratios of the reactants at 1500 °C. The surface morphology shows that as the C/Si ratio decreases, the SiC particle protrusions become more evident. This morphology evolution demonstrates the promoting effect of a higher silicon content in the precursor on SiC grain growth under consistent carbothermal reduction conditions.

Figures 2(a) and 2(b) presents a TEM image of H-SiC/C NFs-S1500-71, clearly revealing their hollow architecture. The fibers have an average diameter of approximately 200 nm with a wall thickness of approximately 60 nm. High-resolution TEM (Fig. 2(c)) revealed distinct lattice fringes with an interplanar spacing of 0.25 nm, corresponding to the (111) plane of 3C-SiC. Well-defined carbon lattice fringes are not observed on the fiber surface, which is attributed to the low degree of graphitization resulting from the relatively moderate heat-treatment temperature. The selected-area electron diffraction (SAED) pattern in Fig. 2(d) shows a set of concentric rings consisting of discrete diffraction spots resulting from the superposition of diffraction spots from numerous randomly oriented SiC grains. The polycrystalline nature of the H-SiC/C NFs was confirmed. Elemental mapping (Figs. 2(e)–2(h)) reveals that Si and C are predominantly distributed within the shell region, further confirming the hollow morphology of the SiC/C fibers in S1500. A minor oxygen signal is also detected, originating from the formation of a small amount of SiO_2 during the high-temperature process.

Figure 2(i) presents the XRD patterns of the H-SiC/C NFs. All the samples exhibit a broad diffraction peak near 25°, which is attributed to an amorphous SiO_2 phase. The distinct diffraction peaks observed at 35.6°, 59.9°, and 71.7° correspond to the (111), (220), and (311) crystal planes of 3C-SiC (JCPDS No. 75-0254), respectively. The noticeable increase in peak intensity with increasing heat treatment temperature indicates improved crystallinity of SiC at higher temperatures. A weak diffraction feature near 34° is associated with stacking faults (SFs) in the 3C-SiC crystal structure [26]. In the Raman spectra (Fig. 2(j)), the two broad peaks located at 1344 and 1582 cm^{-1} are assigned to the D-band (defective carbon) and G-band (carbon atoms with sp^2 hybridization), respectively. The increase in the I_D/I_G ratio with increasing temperature suggests a reduction in graphitic order within the carbon matrix, resulting from its consumption during the carbothermal reduction process to form SiC. XPS analysis was conducted to further characterize the surface chemistry (Figs. 2(k)–2(n) and Fig. S4 in the ESM). The survey spectrum (Fig. 2(k)) confirms the presence of C, Si, and O as the primary elements. The high-resolution C 1s spectrum (Fig. 2(l), Figs. S4(a) and S4(d)

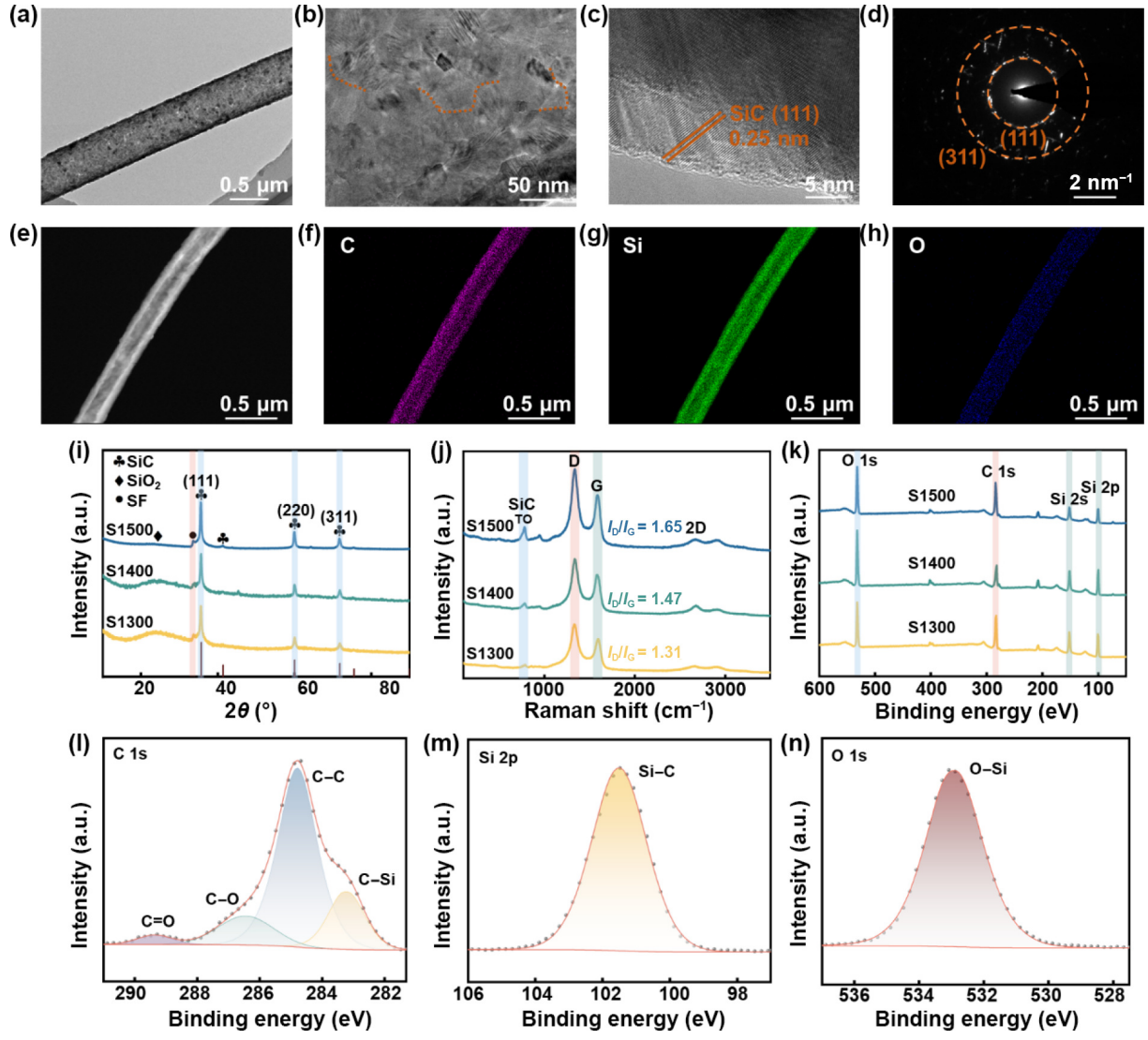

Fig. 2 (a–c) TEM images, (d) SAED, and (e–h) element mapping analysis of H-SiC/C NFs-S1500, (i) XRD patterns, (j) Raman spectra, (k) XPS spectra of different H-SiC/C NFs-S1500, and high-resolution XPS spectra of (l) C 1s, (m) Si 2p, and (n) O 1s for H-SiC/C NFs-S1500.

in the ESM) can be deconvoluted into four components centered at 284.79 eV (C–C, sp^3), 283.21 eV (C–Si), 286.45 eV (C–O), and 289.37 eV (C=O). The weak intensities of the C–O and C=O peaks are likely attributable to surface adventitious carbon and oxidation. The Si 2p spectrum (Fig. 2(m) and Figs. S4(b) and S4(e) in the ESM) is dominated by the Si–C bond at 101.20 eV, whereas the O 1s spectrum (Fig. 2(n), Figs. S4(c) and S4(f) in the ESM) shows a predominant peak corresponding to the O–Si bond at 533.15 eV, which is consistent with the presence of a trace SiO_2 phase in the composites and is consistent with our XRD results. The O–C component at 532.04 eV also likely originates from surface contaminants. Thermogravimetric analysis of H-SiC/C NFs-S1500 (Fig. S5 in the ESM) confirmed the excellent thermal stability of the H-SiC/C nanofibers. Upon heating to 1000 °C, sample S1300 exhibited a minimal mass gain of less than 1%, which was attributed to the formation of a protective SiO_2 layer through the reaction between trace oxygen adsorbed in the hollow fiber and SiC. In contrast, the weights of S1400 and S1500 remain basically unchanged. These results collectively demonstrate that the H-SiC/C nanofibers possess robust thermal stability, which is a key advantage for their application in high-temperature environments.

The remarkable elasticity and fatigue resistance of the H-SiC/C NF aerogel were confirmed through cyclic compression tests. Figure S6(a) in the ESM shows photographs of the aerogel before and after 50% strain. The aerogel fully recovers its original morphology without any surface cracking after being subjected to 50% compression, demonstrating its good elasticity. Figures S6(b) and S6(c) in the ESM shows the stress–strain curves of the aerogel under different maximum strains and the stress-cycle curves of 100 loading–unloading cycles under 30% maximum strain. The corresponding stress–strain curves reveal a linear elastic response up to 50% strain with no significant plastic deformation, indicating outstanding structural resilience. Furthermore, the regular and consistent pattern observed over 100 loading–unloading cycles at 30% strain confirms the aerogel's remarkable structural stability and fatigue resistance. Collectively, these results provide evidence for the elastic properties of our H-SiC/C NF aerogel.

3.2 Electromagnetic wave absorption performance of H-SiC/C NFs

The electromagnetic wave absorption performance of composites is governed by their composition and microstructure. To evaluate these characteristics, H-SiC/C NFs were uniformly blended with

paraffin and pressed into annular samples for coaxial transmission line measurements. As shown in Fig. S7 in the ESM, the real part (μ') of the permeability for H-SiC/C NFs remains at 1, whereas the imaginary part (μ'') is nearly 0 across the 2–18 GHz band. This results in negligible magnetic loss, confirming its minimal contribution to electromagnetic wave absorption. Therefore, our subsequent analysis focused primarily on the complex permittivity. As shown in Fig. 3(a) and Fig. S8 in the ESM, all samples exhibit frequency dispersion behavior, where the real part of the permittivity (ε') decreases with increasing frequency, which is attributed to the lag of polarization relative to the alternating electric field at higher frequencies [27]. When the C : Si ratio of the precursor is held constant, ε' decreases progressively with increasing heat-treatment temperature. This trend results from enhanced formation of the low-permittivity SiC phase at elevated temperatures, where a dense SiC layer develops on and within the fibers, consuming the high-permittivity carbon matrix and thereby reducing the overall dielectric constant. In addition, the influence of the precursor C/Si ratio on the electromagnetic properties of H-SiC/C NFs was investigated. At a heat treatment temperature of 1500 °C, samples prepared with higher C : Si ratios presented greater ε' values, as the excess carbon phase retained after the reaction significantly increased the electromagnetic wave storage capacity of the H-SiC/C NFs. As shown in Fig. 3(b), the ε'' value of S1500-71 exceeds that of S1400 and approaches that of S1500-91, indicating an enhanced dielectric loss capability. This conclusion is further supported by the corresponding dielectric loss tangent ($\tan\delta_\varepsilon$) and attenuation constant (α) of S1500-71, as presented in Fig. 3(c) and Fig. S9 in the ESM. A detailed investigation of the polarization relaxation was enabled by analyzing the Cole–Cole plots. The plot for S1500 at 15 wt% filler loading (Fig. S10 in the ESM) displays multiple distinct semicircles, indicating a broader distribution of relaxation processes and a significantly stronger interfacial polarization than those of the other samples. This enhanced polarization is attributed to the abundant and well-defined SiC/C heterointerfaces formed under the optimized high-temperature treatment. To quantitatively analyze the dissipation mechanisms, we measured the DC conductivity of S1300, S1400, and S1500 at a fixed filler loading of 15 wt% and calculated the respective conduction loss (ε_c'') and polarization loss (ε_p'') contributions on the basis of Debye theory. The results (Figs. S11 and S12 in the ESM) indicate that a higher heat-treatment temperature leads to a pronounced decrease in ε_c''. This trend is attributed to the in situ formation of more SiC and the concomitant consumption of conductive carbon, which collectively reduce the overall electrical conductivity of the material (Table S3 in the ESM). Similarly, for the samples treated at 1500 °C, a lower initial C/Si ratio further promoted the formation of the low-conductivity SiC phase, thereby resulting in an even lower ε_c''. Notably, the ε_c'' values for all samples are several orders of magnitude lower than the total dielectric loss (ε''), indicating that conduction loss plays a negligible role. Therefore, the dominant dissipation mechanism is interface and dipole polarization, which are induced by the SiC/C

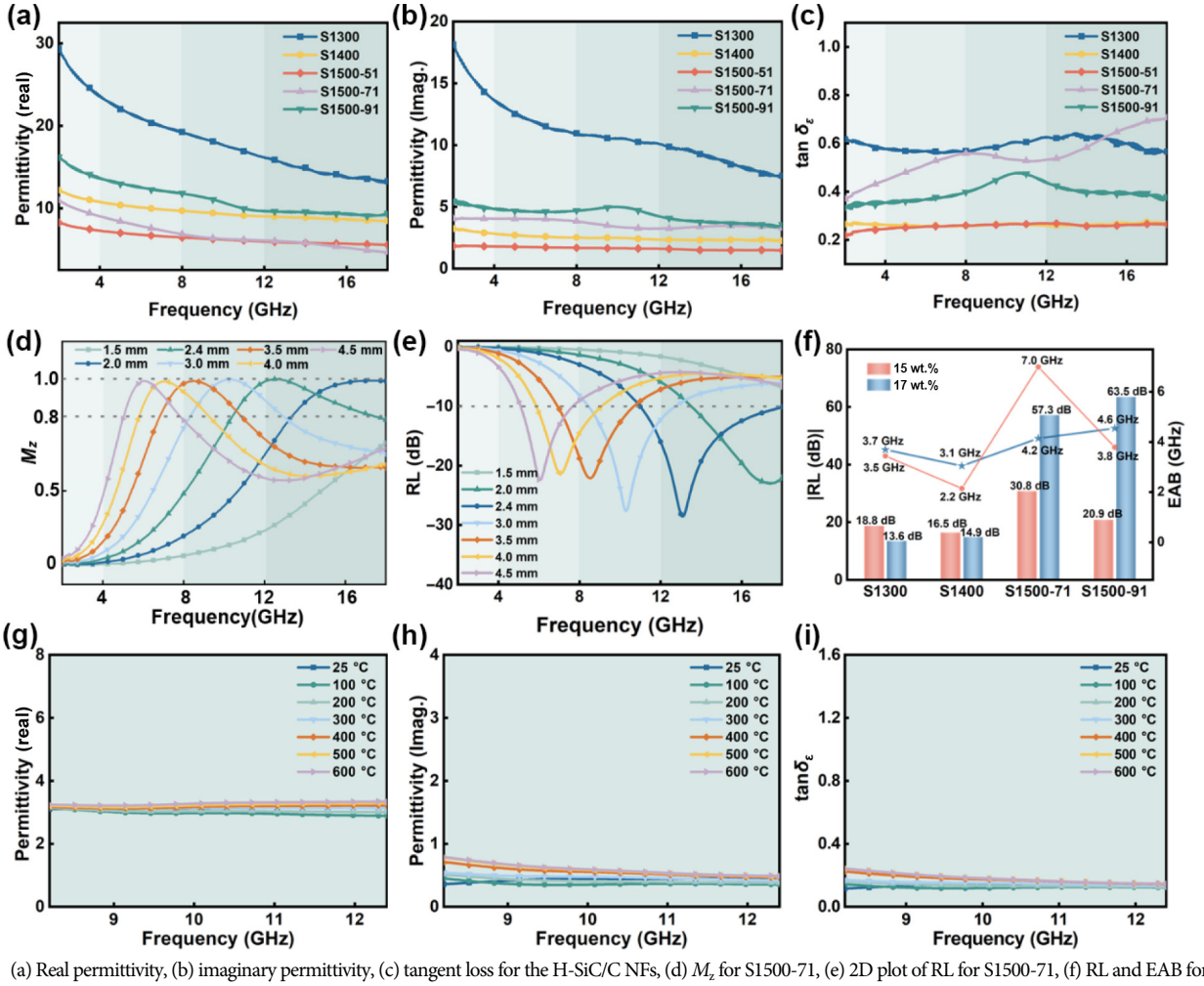

Fig. 3 (a) Real permittivity, (b) imaginary permittivity, (c) tangent loss for the H-SiC/C NFs, (d) M_z for S1500-71, (e) 2D plot of RL for S1500-71, (f) RL and EAB for the H-SiC/C NFs, (g) real permittivity (ε'), (h) imaginary permittivity (ε''), (i) tangent loss ($\tan\delta_\varepsilon$) for S1500-71 at elevated temperature.

heterointerfaces and defects under an alternating electromagnetic field. This conclusion is further supported by the distinct relaxation peaks observed in the ε_p'' curves. Polarization loss is governed by factors such as charge migration capability and defect density. Combined with ICP, XRD, and Raman analyses, we observe that as the heat-treatment temperature increases, the SiC content increases significantly (as evidenced by increasing Si content), leading to more abundant SiC/C interfaces. Concurrently, the increase in the I_D/I_G ratio from the Raman spectra indicates a higher concentration of carbon defects. These factors collectively increase the degree of polarization loss, which explains why the ε_p'' of S1500 exceeds that of S1400. The S1300 sample, with its higher residual carbon content, consequently possesses a much higher complex permittivity and DC conductivity than S1400 and S1500. Furthermore, the defects in this carbon matrix generate strong polarization loss, which is the direct reason for its significantly elevated ε_p'' compared with those of the other samples.

These results suggest that the SiC and carbon phases in S1500-71 approach an appropriate ratio, which enhances electromagnetic wave dissipation while maintaining favorable impedance matching. These results demonstrate that the complex permittivity of H-SiC/C NFs can be effectively tuned by controlling the precursor C:Si ratio and the heat-treatment temperature, enabling optimization of the electromagnetic parameters toward the theoretically desirable range for high-performance absorption [18]. Figure S13 in the ESM shows a comparison between the complex permittivity of sample S1500 and that of an ideal absorber. The analysis reveals that the optimal reflection loss is achieved when both the real and imaginary parts of the sample's permittivity are in close agreement with those of the ideal absorber. This is clearly demonstrated by S1500-71 at 12.5 GHz and S1500-91 at 17.4 GHz, which exhibit the lowest reflection loss at their respective frequencies. These results confirm the significant guiding role of the ideal dispersion curve in designing high-performance electromagnetic wave absorbing materials.

As illustrated in Fig. 3(d), sample S1500-71 exhibited optimal impedance matching at a thickness of approximately 2.4 mm, with a normalized characteristic impedance (M_z) exceeding 0.8 across the 11–18 GHz frequency range. The dissipation of reflected electromagnetic waves is also significantly influenced by the macroscopic geometric structure, which can be modeled via the $\lambda/4$ cancellation theory. The $\lambda/4$ model enhances electromagnetic wave absorption by establishing a π phase difference between waves reflected from the front and back interfaces, leading to their cancellation. As shown in Fig. S14 in the ESM, the experimental data for S1500 agree well with the theoretical curve across the entire 2–18 GHz range, validating the model. Additionally, for materials characterized predominantly by dielectric loss, the experimental values are slightly higher than the theoretical values. This discrepancy becomes more pronounced with increasing $\tan\delta_\varepsilon$.

The electromagnetic wave absorption performance was evaluated via two key metrics, namely, the minimum reflection loss (RL_{min}) and the effective absorption bandwidth (EAB), which are defined as the frequency range over which the RL values fall below −10 dB. These results indicate that the electromagnetic wave absorption properties of H-SiC/C NF composites are strongly influenced by the heat treatment temperature, precursor C:Si ratio, and filler loading. Among the samples investigated (Figs. S15 and S16 in the ESM), S1500-71 delivered the widest EAB and the lowest RL_{min}, indicating the best overall absorption performance. As summarized in Fig. 3(e), S1500-71 loaded at 15 wt% exhibited an RL_{min} of −30.8 dB and an EAB of 7.0 GHz at a thickness of 2.4 mm. Figure 3(f) further shows the broadband electromagnetic wave absorption capability of H-SiC/C NFs-S1500 across the 2–18 GHz range, highlighting their exceptional energy dissipation performance. This superior behavior stems from the synergistic effects of its tailored composition and microstructure. In contrast, an insufficient carbothermal reduction temperature or an excessively high C : Si ratio leads to incomplete conversion of carbon, resulting in an overly high permittivity and consequent impedance mismatch. Therefore, S1500-71 features an optimal architecture where abundant SiC grains are interlaced with a residual carbon matrix, creating numerous heterogeneous interfaces. Furthermore, the hollow fiber morphology collectively enhances impedance matching, thereby contributing to excellent electromagnetic wave absorption performance.

SiC has significant advantages for high-temperature electromagnetic wave absorption applications owing to its excellent high-temperature resistance to oxidation, stable dielectric properties, and tunable loss mechanisms. To evaluate the high-temperature electromagnetic wave absorption performance of H-SiC/C NFs, the complex permittivity was measured via the waveguide method within the X-band (8.2–12.4 GHz) over a temperature range of 25–600 °C (Fig. S17 in the ESM). As shown in Figs. 3(g)–3(i), ε', ε'', and $\tan\delta_\varepsilon$ of S1500 remain stable with increasing temperature. The slight increase observed at elevated temperatures can be attributed primarily to the shortening of the relaxation time, as described by Eqs. (5) and (6). These results confirm the excellent dielectric stability of the H-SiC/C NFs, underscoring their significant application potential for high-temperature electromagnetic wave absorption.

Optimal impedance matching is crucial for minimizing electromagnetic wave reflection and maximizing energy dissipation. The matching efficiency is quantified by the normalized impedance modulus (M_z) (Eq. (3)). Theoretically, perfect impedance matching ($M_z = 1$) ensures full transmission of the incident wave into the absorber, whereas values approaching unity indicate improved matching behavior. Notably, the frequency corresponding to the RL_{min} systematically aligns with the $M_z = 1$ condition, irrespective of absorber thickness. This consistent correspondence confirms that ideal impedance matching is a fundamental prerequisite for achieving optimal electromagnetic absorption performance. In practice, the range $0.8 \le M_z$ is regarded as the effective operating window for efficient absorption [18]. As shown in Figs. 4(a)–4(c) and Fig. S18 in the ESM, the white dashed contours ($M_z = 0.8$–1) delineate regions of favorable impedance matching. At a filler loading of 15 wt%, S1500-71 exhibited the best impedance matching characteristics, with a maximum matching bandwidth of 7.0 GHz. Spatial correlation analysis confirms that the EAB coincides with the $M_z = 0.8$–1 region, demonstrating a deterministic relationship between interfacial impedance alignment and electromagnetic energy conversion efficiency.

The electromagnetic wave absorption properties of the S1300-S1500 composites with a filler loading of 15 wt% are summarized in Figs. 4(d)–4(f). The S1500 sample exhibits superior performance, achieving an RL_{min} of −30.8 dB at 11.7 GHz with a matching thickness of 2.4 mm, alongside an EAB of 7.0 GHz (11.0–18.0 GHz). In contrast, S1300 and S1400 show limited absorption, with higher RL_{min} values of −18.7 dB and narrower EABs of 3.7 GHz. Furthermore, a systematic low-frequency shift of the RL_{min} peak is observed with increasing thickness, a trend that aligns with the quarter-wavelength cancellation model wherein the optimal absorption frequency is inversely proportional to the thickness [28].

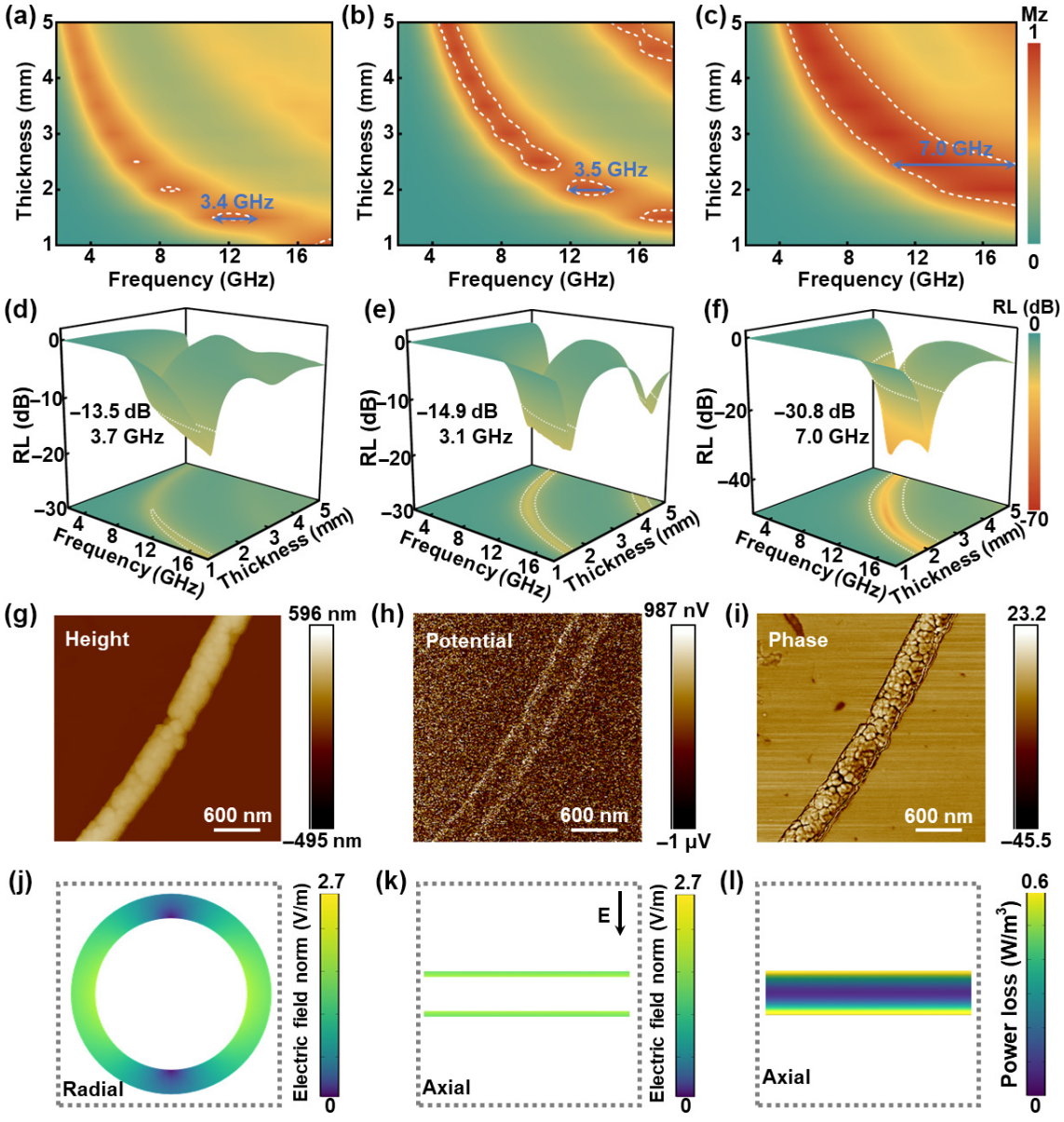

Fig. 4 2D plots of M_z and 3D plots of RL for H-SiC/C (a, d) S1300, (b, e) S1400, (c, f) S1500, the KPFM morphology of (g) height, (h) surface potential difference, (i) phase for the H-SiC/C NFs-S1500-71, (j, k) the electric field norm and (l) power loss density of the H-SiC/C NFs in the simulation results.

Kelvin probe force microscopy (KPFM) was employed to characterize the surface potential distribution of H-SiC/C NFs-S1500-71. As shown in Figs 4(g)–4(i), the potential distribution is nonuniform, with higher surface potential values at the fiber edges and lower values in the central region. This potential gradient provides direct evidence of interfacial polarization, which promotes the accumulation of space charges and leads to the formation of microcapacitor-like structures across the fiber. Figure 4(i) shows the phase distribution on the fiber surface, revealing a dense arrangement of SiC grains that contribute to abundant heterogeneous interfaces. The electromagnetic interaction between the H-SiC/C NFs and high-frequency alternating fields was further investigated via finite element analysis, from which the electric field norm and power loss density were derived. As illustrated in Figs. 4(j)–4(l), the potential difference induced across the shell of the H-SiC/C NFs under an applied electric field is consistent with the KPFM measurements, confirming that the hollow architecture enhances interfacial polarization.

3.3 Electromagnetic wave absorption mechanism in H-SiC/C NFs

To evaluate the radar stealth performance of the H-SiC/C NFs, their monostatic radar cross section (RCS) at 11.7 GHz was simulated via the finite element method. The analytical model schematic is shown in Fig. S19 in the ESM, which consists of a 2.4 mm thick H-SiC/C NF coating applied to a square perfect electric conductor (PEC) substrate (300 mm × 300 mm × 5 mm). The model was irradiated along the Z-axis at a fixed angle (φ = 0°, θ = 0°), and the backscattered signals were recorded across polar angles (θ) ranging from −90° to 90°. The simulated 3D RCS patterns for S1300-S1500 are presented in Figs 5(a)–5(c), revealing that S1500 has a lower scattering cross-section in all directions than the other two samples do. Relative to the bare PEC substrate, the S1500-coated model achieves an RCS reduction of 37.3 dB·m^2 at θ = 0°, whereas the reduction for the S1300-coated model is only 2.8 dB·m^2 (Fig. 5(d)). These simulations verify the great promise of H-SiC/C NF composites for electromagnetic wave

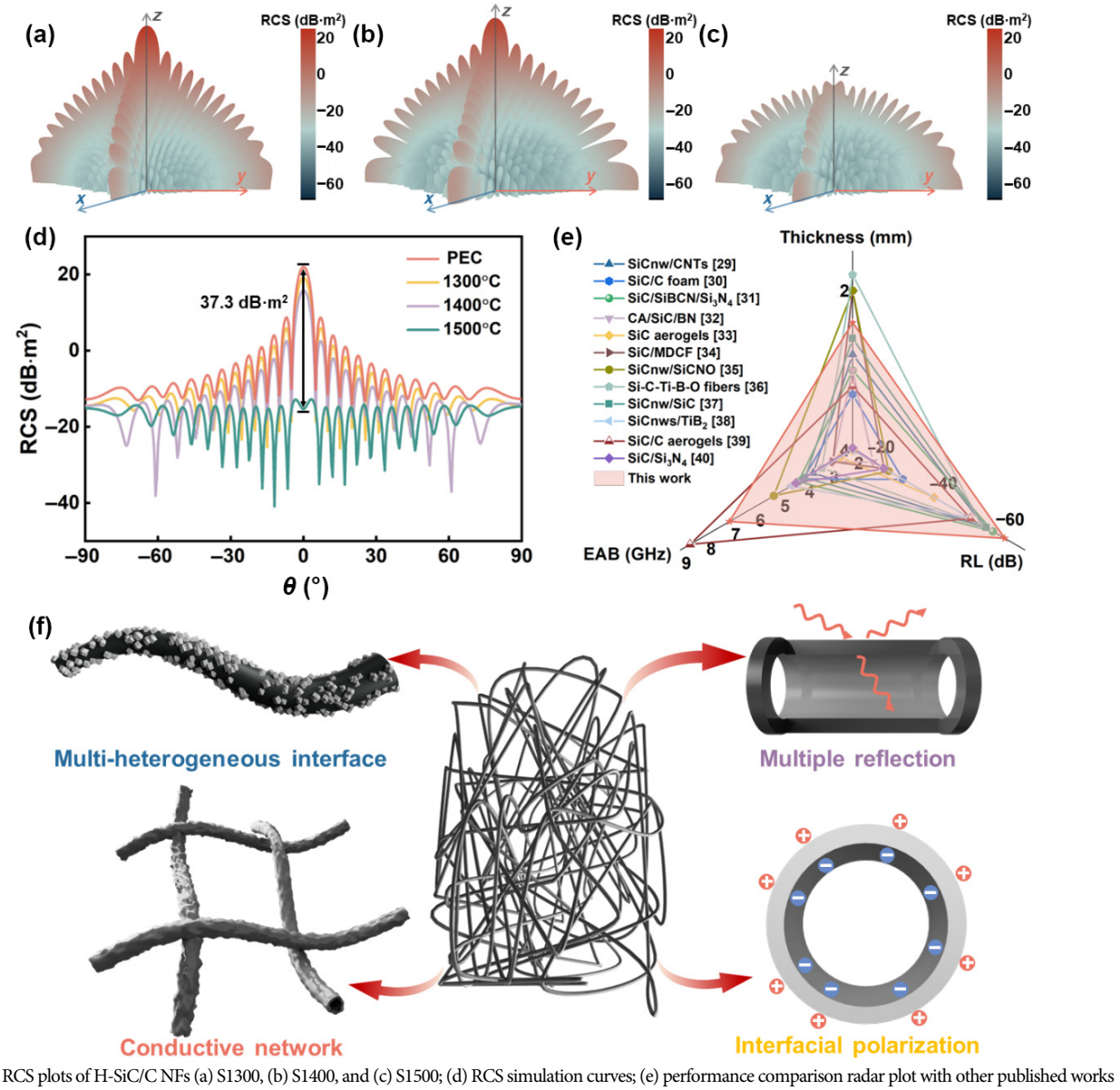

Fig. 5 3D RCS plots of H-SiC/C NFs (a) S1300, (b) S1400, and (c) S1500; (d) RCS simulation curves; (e) performance comparison radar plot with other published works [29–40]; (f) schematic of the electromagnetic wave absorption mechanism of the H-SiC/C NFs.

absorption, which can be achieved by precisely optimizing the synthesis parameters.

In summary, the H-SiC/C NFs demonstrate exceptional electromagnetic wave absorption compared with other methods (Fig. 5(e) and Table S2 in the ESM) [29–35], especially in the ultrawide EAB and RL. The underlying absorption mechanism can be attributed to the synergistic effect of several key factors, as schematically illustrated in Fig. 5(f). First, the hollow architecture of the H-SiC/C NFs optimizes the impedance matching between the material and electromagnetic waves and effectively reduces electromagnetic wave reflection. Second, the overlapping H-SiC/C NFs form an interconnected conductive network, which considerably enhances conduction loss. Third, the abundant heterogeneous interfaces between SiC and carbon distributed on the fiber surface further contribute to polarization loss, collectively increasing the overall electromagnetic energy dissipation capability.

4 Conclusions

In this work, a AgNW@PVA aerogel was synthesized via a hydrothermal reaction and subsequently employed as a precursor to successfully fabricate hierarchical SiC/C hollow nanofiber composites through high-temperature carbonization combined with silicon vapor deposition. The electromagnetic properties of the materials were effectively regulated by controlling the carbothermal reduction temperature and the C/Si ratio. The composite features a fiber shell composed of SiC grains embedded in a carbon matrix and an internal hollow structure, which collectively enhance the thermal stability and impedance matching capability, thereby improving the electromagnetic wave absorption performance. The optimized composite has an RL_{min} of −63.5 dB with an EAB of 4.6 GHz at a thickness of 1.4 mm (S1500-91) and an EAB of 7.0 GHz with an RL_{min} of −30.8 dB at a thickness of 2.4 mm (S1500-71). These results provide a foundation for the development of electromagnetic wave absorbers suitable for high-temperature applications.

Acknowledgements

This work was supported by the National Natural Science Foundation of China (Nos. 22575012, 22505056, and 52373259)

and the Research Funding of Hangzhou International Innovation Institute of Beihang University (No. 2024KQ130). The authors also acknowledge the facilities and scientific and technical assistance of the Analysis & Testing Center of Beihang University and the High-Performance Computing Center of Beihang University. The authors would also like to thank the Shiyanjia Lab (www.shiyanjia.com) for XPS characterization.

Availability of data and materials

The data are available from the corresponding author upon reasonable request.

Competing interests

The authors have no competing interests to declare that are relevant to the content of this article.

Electronic Supplementary Material

Supplementary material is available in the online version of this article at https://doi.org/10.26599/JAC.2025.9221225.

References

[1] Liu PB, He ZZ, Li XC, *et al.* Multifunctional hollow carbon microspheres enable superior electromagnetic wave response and corrosion barrier. *Adv Mater* 2025, **37**: 2500646.

[2] Peng HL, Cai B, Zhang Y, *et al.* Radar-terahertz-infrared compatible stealth coaxial silver nanowire@carbon nano-cable aerogel. *Angew Chem Int Ed* 2025, **64**: e202421090.

[3] Zhang KL, Wang Z, Yan YF, *et al.* Dielectric–magnetic manipulation of reduced graphene oxide permittivity for enhanced electromagnetic wave absorption. *J Adv Ceram* 2024, **13**: 1974–1984.

[4] Wang HY, Hu PF, Sun XB, *et al.* Bioinspired disordered aerogel for omnidirectional terahertz response. *Adv Mater* 2025, **37**: 2418889.

[5] Wu ZM, Huang J, Tan YN, *et al.* Transition/rare earth metal co-modified SiC for low-frequency and high-temperature electromagnetic response. *J Adv Ceram* 2025, **14**: 9221164.

[6] Shen Y, Ma ZQ, Yan F, *et al.* Enhanced interfacial polarization loss of FeS/MoS_2@N-doped carbon sandwich-walled nanotubes enables high-performance electromagnetic wave absorption. *Adv Funct Mater* 2025, **35**: 2423947.

[7] Zhang Y, Hu PF, Zhao PY, *et al.* Phosphorus vacancy-induced built-in electric field for electromagnetic properties modulation. *Adv Sci* 2025, **12**: e02857.

[8] Gao Q, Hu P, Xun LC, *et al.* A scalable method allows for the rapid fabrication of C/SiC composites with excellent mechanical properties and ablation resistance. *J Adv Ceram* 2025, **14**: 9221162.

[9] Zhang B, Qu ZY, Ruiz-Agudo C, *et al.* Lightweight magnetic carbon nanotube/cellulose nanofibre aerogels with microstructure engineering for enhanced microwave absorption. *Carbon* 2025, **234**: 120020.

[10] Cai ZX, Su L, Wang HJ, *et al.* Hierarchically assembled carbon microtube@SiC nanowire/Ni nanoparticle aerogel for highly efficient electromagnetic wave absorption and multifunction. *Carbon* 2022, **191**: 227–235.

[11] Wang Y, Wang T, Arandiyan H, *et al.* Advancing catalysts by stacking fault defects for enhanced hydrogen production: A review. *Adv Mater* 2024, **36**: 2313378.

[12] Cheng GM, Chang TH, Qin QQ, *et al.* Mechanical properties of silicon carbide nanowires: Effect of size-dependent defect density. *Nano Lett* 2014, **14**: 754–758.

[13] Zhang B, Cheng JY, Qu ZY, *et al.* From material design to structural optimization: Genetic algorithm-driven magnetic carbon fiber aerogels for broadband microwave absorption. *J Alloys Compd* 2025, **1042**: 183949.

[14] Xia YJ, Zhang Z, Li KF, *et al.* Lightweight and high-strength SiC/MWCNTs nanofibrous aerogel derived from RGO/MWCNTs aerogel for microwave absorption. *Chem Eng J* 2024, **486**: 150417.

[15] Wei J, Zhang YB, Li XT, *et al.* Recent progress in synthesis, growth mechanisms, and electromagnetic wave absorption properties of silicon carbide nanowires. *Ceram Int* 2022, **48**: 35966–35985.

[16] Cai B, Zhou L, Zhao PY, *et al.* Interface-induced dual-pinning mechanism enhances low-frequency electromagnetic wave loss. *Nat Commun* 2024, **15**: 3299.

[17] Zhang Y, Yang SH, Xin Y, *et al.* Designing symmetric gradient honeycomb structures with carbon-coated iron-based composites for high-efficiency microwave absorption. *Nano-Micro Lett* 2024, **16**: 234.

[18] Hou ZL, Gao XS, Zhang JY, *et al.* A perspective on impedance matching and resonance absorption mechanism for electromagnetic wave absorbing. *Carbon* 2024, **222**: 118935.

[19] Qin M, Zhang LM, Wu HJ. Dielectric loss mechanism in electromagnetic wave absorbing materials. *Adv Sci* 2022, **9**: 2105553.

[20] Koo MC, Zhang Y, Cai B, *et al.* Enhancing microwave absorbing properties of C/TiO_2/NiNW composites through built-in electric field effect. *J Mater Sci Technol* 2026, **244**: 102–110.

[21] Xia YX, Gao WW, Gao C. A review on graphene-based electromagnetic functional materials: Electromagnetic wave shielding and absorption. *Adv Funct Mater* 2022, **32**: 2204591.

[22] Liang CM, Hou ZL, Koo MC, *et al.* Modulating electromagnetic response through the regulation of built-in electric fields. *J Mater Sci Technol* 2026, **248**: 126–134.

[23] Zhao PY, Peng HL, Cai B, *et al.* Mechanism decoupling of impedance matching and attenuation enhancement via spatial distribution of loading components. *Adv Funct Mater* 2025: 18479.

[24] Su XG, Gao XY, Wang J, *et al.* Multifunctional broadband electromagnetic wave absorption through structural engineering of hierarchical aerogel-honeycomb metacomposites. *Carbon* 2025, **243**: 120517.

[25] Zeng XJ, Li E, Xia GH, *et al.* Silica-based ceramics toward electromagnetic microwave absorption. *J Eur Ceram Soc* 2021, **41**: 7381–7403.

[26] Zhang HY, Xu YJ, Zhou JG, *et al.* Stacking fault and unoccupied densities of state dependence of electromagnetic wave absorption in SiC nanowires. *J Mater Chem C* 2015, **3**: 4416–4423.

[27] Shen ZZ, Chen JH, Li B, *et al.* Recent progress in SiC nanowires as electromagnetic microwaves absorbing materials. *J Alloys Compd* 2020, **815**: 152388.

[28] Bai YX, Liu DP, Zhou L, *et al.* High-Performance wave loss capability by constructing well-defined hierarchical aerogel framework with strongly coupled carbon/CeO_2 interface. *Chem Eng J* 2025, **504**: 158873.

[29] Mei H, Yang WQ, Zhao X, *et al. In-situ* growth of SiC nanowires@carbon nanotubes on 3D printed metamaterial structures to enhance electromagnetic wave absorption. *Mater Des* 2021, **197**: 109271.

[30] Xiao SS, Mei H, Han DY, *et al.* Ultralight lamellar amorphous carbon foam nanostructured by SiC nanowires for tunable electromagnetic wave absorption. *Carbon* 2017, **122**: 718–725.

[31] Cheng ZL, Liu YS, Ye F, *et al.* Microstructure and EMW absorbing properties of SiC_{nw}/SiBCN-Si_3N_4 ceramics annealed at different temperatures. *J Eur Ceram Soc* 2020, **40**: 1149–1158.

[32] Pan D, Yang G, Abo-Dief HM, *et al.* Vertically aligned silicon carbide nanowires/boron nitride cellulose aerogel networks enhanced thermal conductivity and electromagnetic absorbing of epoxy composites. *Nano-Micro Lett* 2022, **14**: 118.

[33] Yan MY, Cheng XD, Gong LL, *et al.* Growth mechanism and structure regulation of super-elastic SiC aerogels for thermal insulation and electromagnetic wave absorption. *Chem Eng J* 2023, **475**: 146417.

[34] Ye XL, Chen ZF, Ai SF, *et al.* Porous SiC/melamine-derived carbon

foam frameworks with excellent electromagnetic wave absorbing capacity. *J Adv Ceram* 2019, **8**: 479–488.

[35] Yuan KK, Han DY, Liang JF, *et al*. Microwave induced *in situ* formation of SiC nanowires on SiCNO ceramic aerogels with excellent electromagnetic wave absorption performance. *J Adv Ceram* 2021, **10**: 1140–1151.

[36] Kang WF, Zhang QY, Gou YZ. Fabrication of highly crystalline titanium-containing SiC fibers with different boron contents exhibiting excellent electromagnetic wave absorption. *J Mater Sci* 2024, **59**: 2739–2756.

[37] Wang CY, Tang J, Wang ZC, *et al*. Tuning the microstructure of porous SiC_{nw}/SiC fabricated by vat photopolymerization 3D printing for electromagnetic wave absorption. *Ceram Int* 2024, **50**: 7745–7757.

[38] Yan LL, Wang X, Li WC, *et al*. High-temperature resistance and broadband radar absorbers based on SiC nanowires coatings with titanium diboride metasurfaces. *Appl Surf Sci* 2024, **653**: 159383.

[39] Dai D, Lan XL, Wang ZJ. Hierarchical carbon fiber reinforced SiC/C aerogels with efficient electromagnetic wave absorption properties. *Compos Part B Eng* 2023, **248**: 110376.

[40] Dai D, Lan XL, Wu LN, *et al*. Designed fabrication of lightweight SiC/Si_3N_4 aerogels for enhanced electromagnetic wave absorption and thermal insulation. *J Alloys Compd* 2022, **901**: 163651.